Resonant-Coherent Excitation of Channeled Ions

F. J. García de Abajo[1] and V. H. Ponce[2]

[1] *Centro Mixto CSIC-UPV/EHU and Donostia International Physics Center (DIPC), Manuel de Lardizábal 4, 20018 San Sebastián, Spain*
[2] *Centro Atómico Bariloche, Comisión Nacional de Energía Atómica, 8400 San Carlos de Bariloche, Argentina*

Abstract

A theoretical description of charge transfer processes during ion channeling is presented, with special emphasis on coherent transitions originating in the periodicity of the crystal lattice. The interplay between coherent interaction with the periodic crystal lattice potential and inelastic electron–electron collisions is shown to be crucial in both intra-ionic transitions and electron loss from the ion. The mixing and energy shifting of the electronic states of the projectile is introduced *via* both the crystal potential, averaged over the ion trajectory, and the induced wake potential. A full calculation of the various electronic transitions occurring during ion channeling is offered and comparison with measured survival charge fractions is shown to result in excellent agreement when a detailed account of the necessary ingredients is incorporated, including the time evolution of the ion trajectory along the channel. One of these ingredients is electron loss from the projectile due to coherent interaction with the crystal lattice. It is shown, in particular, that the angular distribution of coherently emitted electrons is directed along preferential directions determined by the reciprocal crystal lattice.

Contents

ADVANCES IN QUANTUM CHEMISTRY, VOLUME 46
ISSN: 0065-3276 DOI 10.1016/S0065-3276(04)46003-1

1. INTRODUCTION

An ion moving under channeling conditions inside a crystal or near its surface is subject to the perturbation of both the static potential set up by the ordered atoms of the crystal and the induced potential originating in the charge density fluctuations produced by the presence of the ion. The periodic components of the crystal potential may induce transitions in the internal electronic state of the ion (coherent electron excitation [1–4] and electron capture and loss [5,6]) while leaving the state of the target unchanged. However, the induced potential produces changes in the electronic state of the target itself, like the creation of electron–hole pairs and collective plasmon modes, and this can occur either without modifying the internal electronic state of the projectile or accompanying simultaneous changes in the latter. The inelastic nature of the induced potential results in a retarding force acting back on the ion and producing stopping.

A theory suitable to deal with all of these mechanisms of charge transfer between projectile and target will be derived from first principles in this chapter, and will be illustrated with examples of numerical calculation and comparison with experiments. Special emphasis will be placed on the so-called resonant-coherent excitation (RCE), i.e., the excitation of the internal electronic state of the ion caused by the spatial periodicity of the lattice, which is experienced by the moving ion as a periodicity in time, enabling transitions of frequency corresponding to different harmonics contributing to the crystal potential. Okorokov [7] predicted this effect and later reported on experimental evidence for He^+ ions axially channeled in Ag [8,9]. Unsuccessful attempts to reproduce this result [10–12] led Datz *et al.* [1–4] to obtain the first solid experimental evidence of RCE for heavier ions, attributing previous negative results to the short lifetime of excited states of channeled He^+ ions, whose size is comparable to the channel width. In a set of elegant experiments, these authors observed the reduction in the transmission of fixed charge state hydrogenic ions of atomic number $Z_1 = 5–9$, axially channeled in Au and Ag crystals, when one of the harmonics of the crystal potential matches the energy difference between the electron ground state and some excited state, the latter being more easily ionizable than the former due to stronger interaction with the solid.

A large deal of work has been devoted to experimentally study charge state fractions of ions traversing solids under axial [13] and planar [13,14] channeling conditions, or scattered after surface channeling [15,16]. Most of these studies share in common the use of large velocities $v = 2–100$ a.u., which entail a comparatively weak interaction with the solid, thereby ensuring that the electronic states of the ions live long enough to exhibit well-defined resonances. However, long-lived states are also possible at lower ion velocities when the electronic states of the projectile lie inside a band gap of the crystal [17]. Some of the most relevant experimental work in

connection to charge transfer and RCE during ion channeling is reviewed in Table 1.

In order to study the charge state of channeled ions, it is convenient to separate the interaction between the moving ion and the crystal into two distinct contributions to the total potential: the static crystal potential, consisting of the interaction with all electrons and nuclei in the unperturbed medium, and the induced potential resulting from the distortion produced in the medium by the projectile. Notice that the so-called wake potential [48–51] corresponds to the part of the induced potential related to the perturbation of valence band electrons.

Under axial, planar, or surface channeling conditions, the trajectory forms a glancing angle with respect to the channel, and thus, the ion motion perpendicular to the crystal axis, plane, or surface, in each case, can be decoupled from the fast motion along the remaining direction *parallel* to the channel, leading to the concept of the so-called continuous axial, planar, or surface potential, respectively [52]. These are nothing but the average of the crystal potential over trajectories parallel to the channel with fixed impact parameter [32,52,53].

1.1. Ingredients needed to describe charge exchange during channeling

To be more specific, the following ingredients need to be incorporated to the theory: intra-ionic transitions connecting electronic bound states of the ion *via* frequency components of the crystal potential (Section 1.1.1); splitting and mixing of electronic states, originating in the net electric field created by both the induced wake potential and the continuous axial, planar, or surface potential, in each case [54,55] (Section 1.1.2); electron loss due to coherent excitation to the continuum (Section 1.1.3); non-coherent electron–electron collisions leading to (de-)excitation and electron loss (Section 1.1.4); electron capture from occupied states of the target (Section 1.1.5); and the ion trajectory, which accompanies the dynamical evolution of the electronic state of the ion (Section 1.1.6).

1.1.1. Resonant-coherent excitation

RCE can be regarded as an elastic process in the laboratory frame, in which the lattice acts like a source of momentum. RCE, in order to take place, requires that the energy difference between bound states lies near some of the harmonic energies of the crystal potential. The effect of the rest of the harmonics is negligible. RCE has been observed under both axial [1–3] and planar [4,43] channeling conditions, and more recently also in surface channeling conditions [17,19,27,29,35]. Experimental corroboration exists that some harmonics can be suppressed due to destructive interference

Table 1. Experimental studies of resonant-coherent excitation and charge state fractions of ions channeled through thin films and surfaces, ordered by projectile atomic number

Authors	Projectile → Target	Energy, MeV (Velocity, a.u.)	Trajectory
Gaillard *et al.* (1976) [13]	H^+ → Au, Ni	0.5–2 (4.5–8.9)	(111) plane[a–d]
			(110) plane[b–d]
			⟨110⟩ axis[c–e]
Winter *et al.* (1991) [18]	H^+ → Al	0.1–1.2 (2–6.9)	(111) surface[c,d]
Auth *et al.* (1997) [17–20]	H → LiF	(0.35–0.57)	(100) surface[f,g]
Hecht *et al.*(1998) [21,20]	H → LiF	(0.28–0.6)	(100) surface[g,h]
Berry *et al.* (1974) [11]	He^+ → Au	0.26–0.34 (1.6–1.8)	⟨110⟩ axis[d]
Kimura *et al.* (1988) [22]	He^+ → SnTe	0.5–1.9 (2.2–4.4)	(100) surface[d,i]
Fujii *et al.* (1989–1990) [23,24]	He^+ → Au	0.5–1.9 (2.2–4.4)	(100) plane[a,d,j]
	He^+ → SnTe		(100) plane[a,d,j]
Fujii *et al.* (1991) [25]	He^+ → SnTe	0.5–1.9 (2.2–4.4)	(100) surface[d]
Kimura *et al.* (1992) [16]	$He^{+,2+}$ → SnTe	0.5 (2.2)	(100) surface[d,k]
Narumi *et al.* (1995) [26]	Li^+–Li^{3+} → SnTe	3.2 (4.3)	(100) surface[d,k]
Kimura *et al.* (1996–1998) [27–30]	B^{4+} → SnTe	4.5–6.5 (4.1–4.9)	(100) surface[h,l–o]
Datz *et al.* (1978–1979) [1–3]	C^{5+} → Au	16.5–24.7 (7.4–9.1)	⟨100⟩ axis[h,m]
Krause *et al.* (1993) [31]	C^{5+} → Si	5–35 (4.1–10.8)	⟨111⟩ axis[h,p]
Krause *et al.* (1994) [32]	C^{3+}–C^{6+} → Si	10–30 (5.8–10)	⟨100⟩ axis[l]
Datz *et al.* (1996) [33]	C^{6+} → Si	26 (9.3)	(100) plane[q]
Datz *et al.* (1978–1979) [1–3]	N^{6+} → Au	34.5–42 (9.9–11)	⟨100⟩ axis[h,m]
	N^{6+} → Au	16–35 (6.8–10)	⟨111⟩ axis[h,m]
Datz *et al.* (1979–1980) [3,4]	N^{6+} → Au	15–27 (6.5–8.8)	(100) plane[h]
	N^{5+} → Au	15–20 (6.5–7.6)	(100) plane[h]
Krause *et al.* (1993) [31]	N^{6+} → Si	13–42 (6.1–10.9)	⟨111⟩ axis[h,p]
Datz *et al.*(1995) [34]	N^{6+} → Au	45.5 (11.4)	(100) plane[h,r]
Hatke *et al.* (1997–1998) [35,36]	N^{6+} → Pt	21.8–23 (7.9–8.1)	(110) surface[h,r]
Datz *et al.* (1978–1979) [1–3]	O^{7+} → Au	38–45 (9.7–10.6)	⟨110⟩ axis[h,m]
Datz (1979) [3]	O^{5+}–O^{8+} → Au	40 (10)	⟨110⟩ axis[h]
Azuma *et al.* (1996) [14]	O^{6+}–O^{8+} → Si	103.5 (16.1)	(110) plane[d,q]
Datz *et al.* (1978–1979) [1–3]	F^{8+} → Au	34.6–45 (8.5–9.7)	⟨100⟩ axis[h,m]
	F^{7+} → Au	31–39.5 (8.1–9.1)	⟨100⟩ axis[h,m]
Fujimoto *et al.* (1988) [37]	Ne^{9+} → Au	75–100 (12.2–14.1)	⟨111⟩ axis[a,f]

Datz *et al.* (1991) [38]	$Mg^{11+} \rightarrow Au$	150–167 (15.7–16.6)	$\langle 100 \rangle$ axis[h,s]
Datz *et al.* (1995) [34]	$Mg^{11+} \rightarrow Ni$	607.8 (31.6)	$\langle 100 \rangle$ axis[h]
Datz *et al.* (1996) [33]	$Mg^{11+} \rightarrow Au$	157–178 (5.6–6.0)	$\langle 111 \rangle$ axis[f,h]
Forster *et al.* (1996) [39]	$Si^{13+} \rightarrow Si$	20–24 (5.3–5.8)	$\langle 112 \rangle$ axis [h]
		20–26 (5.3–6.1)	$\langle 111 \rangle$ axis[h]
Azuma *et al.* (1998–1999) [40–43]	$Ar^{17+} \rightarrow Si$	15580 (97)	(100) plane[g,h,l,m,q,t]
			(110) plane
			(111) plane
Azuma *et al.* (2003) [44]	$Ar^{17+} \rightarrow Si$	15580 (97)	(110) plane[f,t,u]
Ito *et al.* (2000–2003) [45,46]	$Ar^{17+} \rightarrow Si$	15580 (97)	(110) plane[f,g,t]
Nakai *et al.* (2003) [47]	$Ar^{17+} \rightarrow Si$	3755 (57.1)	(100) plane[g,h,l,t]
Datz *et al.* (1996) [33]	$Ti^{21+} \rightarrow Si$	225–375 (13.7–17.8)	$\langle 111 \rangle$ axis[r,v]

[a] Comparison with random orientation is offered.
[b] The variation of $[H^0]$ with angle of incidence is also analyzed.
[c] $[H^0]$ charge fractions of the order of 10^{-3}.
[d] RCE not detected.
[e] Amorphous target.
[f] RCE observed through X-ray yield.
[g] Dependence of RCE with respect to the azimuthal angle of incidence.
[h] RCE observed through charge state fractions.
[i] Comparison with transmission data.
[j] Dependence of charge fractions with incidence angle normal to the channel.
[k] Dependence on the angle of incidence.
[l] Analysis of the trajectories included.
[m] Dependence of the RCE and charge state fractions on a slight angular tilt with respect to the channel direction.
[n] Axially channeled ions along the [100] direction in the (001) surface. $B^{4+,5+}$ are detected, since the first electron is rapidly lost.
[o] Effect of surface steps analyzed *via* dependence on angles of incidence/scattering.
[p] Interference effects of the crystal potential in RCE.
[q] 2D maps of the dependence of ion transmission on the direction of emergence.
[r] Dependence of charge fractions on azimutal angle of incidence.
[s] Charge state fractions measured with different angles of acceptance.
[t] Outstanding identification of sublevel contributions to RCE and charge fractions.
[u] RCE detected *via* changes in convoy electron emission yield.

effects [31]. Moreover, both an increase in ionized charge state fractions [1–4,27] and an enhancement in the convoy electron yield on resonance have been reported [56].

When ions of large atomic number are considered (e.g., Mg^{11+}), they have chances to leave the crystal in an excited state after suffering RCE without further ionization, thus leading to the emission of X-rays by radiative de-excitation. This light emission has been experimentally observed [34,37,38, 57] and proved to be polarized in a way related to the channel geometry and the ion trajectory [34].

In a recent experiment, Auth *et al.* [17,19] have combined the detection of this type of light emission with the use of low-velocity ($v \sim 0.5$ a.u.) light projectiles such as H atoms reflected on a LiF surface, taking advantage of the large band gap of this material to minimize charge transfer between surface and projectile, a situation that increases the lifetime of the electronic states involved in the RCE, which is a necessary condition to have a sufficiently sharp resonance.

The theoretical development of RCE started with first-order perturbation treatments [9] and continued by solving a set of coupled-channel equations involving only the bound states relevant to the process [58] (i.e., K and L shells of hydrogenic ions). The observed energy shift and splitting of atomic levels bound to the channeled ions were satisfactorily explained by Crawford and Ritchie [54] in terms of the wake potential [48,49]. Early attempts to describe RCE at surfaces were also reported [59–61]. The shape of the resonance is well understood as originating in the dependence of the splitting along the ion trajectory [34,62,63]. Further analysis has shown a complex dynamical evolution of the electronic states under discussions along the trajectory of the ion [62,64].

1.1.2. Energy mixing and splitting of electronic states

The electronic states of the ion are mixed and energy split by interaction with the target. The resulting new basis of adiabatic states, among which RCE processes can occur, depends on the impact parameter of the ion in the channel, which varies along the trajectory [62]. This may modify the conditions for which RCE takes place, and in particular, this can depend strongly on the ion impact parameter across the channel (see Fig. 1).

1.1.3. Resonant-coherent excitation to the continuum: coherent loss

RCE can take place in such a way that the excited state lies in the continuum, leading to electron coherent loss (CL) [6]. This is similar to what happens in low-energy electron diffraction, where a plane wave is reflected on a surface along directions dictated by both energy conservation and a change in parallel momentum equal to a reciprocal surface lattice vector. Instead, the incoming electron is attached to the ion in the present context, and it

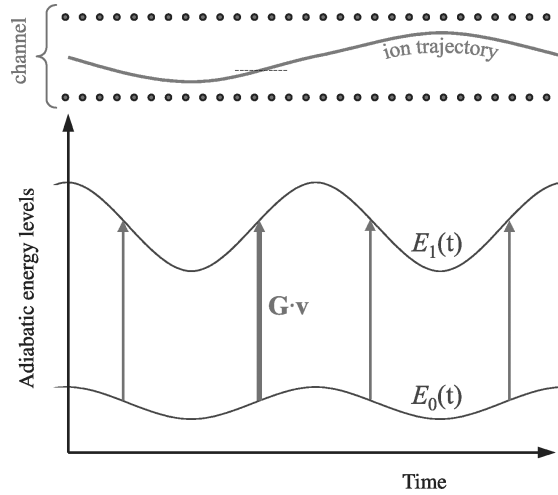

Fig. 1. Schematic representation of the trajectory of the ion as it moves along a channel defined by atomic walls in a crystal (upper part) and evolution of the adiabatic electronic states of the ion (lower part). The energy of the latter depends on the distance of the ion to the atomic walls, and there are certain positions along the trajectory for which the energy difference between two such states are in resonance with some harmonic **G** of the crystal potential (vertical arrows).

represents a finite-size distribution in momentum space centered around the ion velocity [5,65,66]. The bound states of the ion can be de-populated *via* this effect, introducing a width in the electronic adiabatic levels. It has been speculated for the case of surface channeling that coherently emitted electrons should travel with well-defined energy around preferential directions [66]. Experimental evidence of this type of electron emission is still missing. Also, for planar or axial channeling in the bulk, when very thin films and large projectile velocities are considered, the ejected electron may have a mean free path in the solid comparable to the film thickness, so that it may leave the target carrying direct information on the excitation process.

1.1.4. Inelastic processes

The creation of electron–hole pairs and plasmon excitations in the target needs to be considered as well in connection to the simultaneous promotion of a moving ion-bound electron, which can occur by absorbing energy out of the fast ion motion. The theory of this kind of two-electron Auger transitions was developed by Guinea *et al.* [67] to study charge state fractions of ions moving in an electron gas. Their model was extended later by Sols and Flores [65] to include capture from inner shells of target atoms and coherent processes of the sort discussed in Section 1.1.3. In the context of the present work, the importance of two-electron Auger processes in

the resulting charge state of fast-channeled ions was conclusively demonstrated by Datz *et al.* [38].

1.1.5. Electron capture

The ion may capture electrons from the target. In particular, electron capture from inner shells of target atoms may be important when the ion finds itself traveling very close to any plane or string of atoms of the crystal.

There is a fundamental difference between electron capture and two-electron Auger processes on one hand and the RCE and loss discussed in Sections 1.1.1 and 1.1.3 on the other. The latter are produced by periodic components of the static crystal-lattice potential, and hence they are elastic processes from the point of view of the target (i.e., the target does not change its internal state, since it only acts like a reservoir of momentum, while the projectile changes both its internal state and the momentum of its center of mass). Thus, RCE and CL are indeed coherent processes for which keeping track of the phase of the probability amplitudes is important. Quite differently, electron–electron collisions and electron capture are incoherent in the sense that they involve changes of the target state. In practice, the loss of a projectile electron *via* CL is inelastic, since the probability that the electron comes back to its original state is negligible and it will eventually interact inelastically with the solid. The same goes for the hole left behind during electron capture.

1.1.6. The ion trajectory

Finally, the ion moves following a nearly classical trajectory, which is governed by the continuous axial, planar, or surface potential, together with the image potential in the case of surface channeling [66], provided the ion energy is large enough to ensure a relatively negligible stopping.

We will present a formal derivation of the theory needed to deal with charge transfer processes during channeling in Section 2 and calculated results for RCE will be shown and compared with experiments later on in this chapter. Atomic units (a.u., $e = \hbar = m = 1$) will be used from now on, unless otherwise specified.

2. THEORETICAL FRAMEWORK

A semi-classical formalism will be followed to describe the time evolution of the projectile electronic state. The ion trajectory will be governed by the continuous channel potential and considered to be unaffected by charge transfer processes, while the electronic state itself will be described by the Schrödinger equation.

Let us focus, for simplicity, on a hydrogenic ion of atomic number Z_1 moving under planar or surface channeling conditions, so that the position of the projectile nucleus evolves according to $\mathbf{r}_p(t) = (\mathbf{R}_p + \mathbf{v}t, z_p(t))$, where $\mathbf{v}$ stands for the ion velocity parallel to the channel plane or surface. The generalization of this situation to multi-electron ions or axial channeling adds no conceptual difficulty. In what follows, upper case vectors will denote components parallel to the channel or surface, respectively, and z will represent the perpendicular direction. In practice, the time of interaction with the target will be sufficiently small to guarantee that the parallel velocity $\mathbf{v}$ remains nearly constant and the effect of ion energy loss on the trajectory is negligible.

Channeling conditions require that the trajectory forms small angles at any point with the channel direction, and therefore, $z_p(t)$ is a slowly varying function of the time. This permits distinguishing two different time scales: the fast motion along the channel and the slow modulations of the trajectory in the normal direction.

The quantum states of the entire system (ion–target) can be safely separated into two different parts corresponding to the state of the electron bound to the ion and the state of the target, respectively. The state of this composite can be written as

$$|\Phi\rangle = \sum_{\mu n} a_{\mu n}\, \mathrm{e}^{-\mathrm{i}\varepsilon_{\mu n} t} |\mu n\rangle, \tag{1}$$

where $a_{\mu n}$ is the amplitude of stationary state $|\mu n\rangle$ of energy $\varepsilon_{\mu n}$, and μ and n denote electronic and target quantum numbers, respectively. In particular $n = 0$ will refer to the ground state of the target.

The evolution of the composite wave function is described by the Schrödinger equation,

$$(\hat{H}_0 + \hat{U})|\Phi\rangle = \mathrm{i}\frac{\partial}{\partial t}|\Phi\rangle, \tag{2}$$

where $\hat{H}_0$ is the non-interacting part, i.e., $\hat{H}_0|\mu n\rangle = \varepsilon_{\mu n}|\mu n\rangle$, and $\hat{U}$ describes the ion–target interaction. The latter can be written as

$$\hat{U} = Z_1 \hat{V}(\mathbf{r}_p) - \hat{V}(\mathbf{r}_p + \mathbf{r}), \tag{3}$$

where both the target nuclear potential and the electronic degrees of freedom of the target are incorporated in $\hat{V}$, and the dependence on the projectile-electron coordinate $\mathbf{r}$ relative to the ion center of mass comes exclusively *via* the second term.

Part of this interaction is represented by the static crystal potential, which corresponds to the average of $\hat{V}$ in the target ground state $|n = 0\rangle$. Owing to

the periodicity of the crystal in its ground state, one can write

$$V^{\mathrm{C}}(\mathbf{r}_{\mathrm{p}}+\mathbf{r}) = \langle 0|\hat{V}(\mathbf{r}_{\mathrm{p}}+\mathbf{r})|0\rangle = \sum_{\mathbf{G}} V^{\mathrm{C}}_{\mathbf{G},z_{\mathrm{p}}(t)+z}\, \mathrm{e}^{\mathrm{i}\mathbf{G}\cdot(\mathbf{R}_{\mathrm{p}}+\mathbf{R}+\mathbf{v}t)}, \tag{4}$$

where the sum is extended over reciprocal lattice vectors parallel to the surface or channel, $\mathbf{G}$.

The local average value of V^{C} along the trajectory for a given impact parameter z_{p},

$$\bar{V}^{\mathrm{C}}(\mathbf{R}_{\mathrm{p}}+\mathbf{R}, z_{\mathrm{p}}+z) = \sum_{\mathbf{G}\cdot\mathbf{v}=0} V^{\mathrm{C}}_{\mathbf{G},z_{\mathrm{p}}+z}\, \mathrm{e}^{\mathrm{i}\mathbf{G}\cdot(\mathbf{R}_{\mathrm{p}}+\mathbf{R})}, \tag{5}$$

plays an important role in mixing and splitting bound energy levels, and also in determining the ion trajectory.

Projecting equation (2) on the basis of stationary states introduced above, one finds the following infinite set of coupled-channel equations:

$$\mathrm{i}\frac{\mathrm{d}a_{\mu n}}{\mathrm{d}t} = \sum_{\mu' n'} \langle \mu n|\hat{U}|\mu' n'\rangle \exp[\mathrm{i}(\varepsilon_{\mu n} - \varepsilon_{\mu' n'})t] a_{\mu' n'}. \tag{6}$$

It is convenient to define a finite subspace P consisting of the target ground state together with a selected set of relevant bound states of the projectile electron (e.g., K and L shells). The remaining orthogonal subspace Q contains all kinds of excited states of the target and projectile electron states. This separation permits one to reduce equation (6) to a finite set of relevant coupled equations limited to subspace P, which can be solved numerically. This is described in detail in Appendix A, where the following two steps have been followed:

(a) First, the amplitude of each Q state is calculated within first-order perturbation theory, assuming that the P-state amplitudes remain constant during a sufficiently long time interval. This is a reasonable assumption far from resonance, which is the situation discussed in Appendix A. However, when two P states are on resonance, their amplitudes exhibit rapid Rabi oscillations and one has to follow a different procedure: during a short period of time, they can be calculated from equation (6) by neglecting all transitions to Q states; when the resulting oscillating amplitudes are used in the right-hand side of equation (6) to calculate Q-state amplitudes, one obtains the same expressions as in the off-resonance situation (this analysis is a straightforward generalization of Appendix A and it will not be given here).

(b) The Q-state amplitudes calculated in this way are inserted back into equation (6) for $|\mu n\rangle \in P$. Then, the right-hand side of the equation can be rearranged in order to be expressed in terms of the amplitudes of P

states and some coupling rates representing the leakage of electron probability from P due to transitions to Q states. A finite set of equations is obtained for the amplitudes of P states.

The final result, derived in Appendix A, reads

$$\mathrm{i}\frac{\mathrm{d}a_\alpha}{\mathrm{d}t} = \sum_\beta \Sigma_{\alpha\beta}\, \mathrm{e}^{\mathrm{i}(\varepsilon_\alpha-\varepsilon_\beta)t} a_\beta + \sum_{\beta,\mathbf{G}} V^{\mathrm{C}}_{\alpha\beta,\mathbf{G}}\, \mathrm{e}^{\mathrm{i}(\varepsilon_\alpha-\varepsilon_\beta-\mathbf{G}\cdot\mathbf{v})t} a_\beta, \tag{7}$$

where α and β denote the electronic part of P states, and

$$\Sigma_{\alpha\beta} = V_{\alpha\beta} - \frac{\mathrm{i}}{2}(\Gamma^{\mathrm{CL}}_{\alpha\beta} + \Gamma^{\mathrm{Auger}}_{\alpha\beta}) \tag{8}$$

represents complex self-energy matrix elements. Here, the resonant term

$$V^{\mathrm{C}}_{\alpha\beta,\mathbf{G}} = -\langle\alpha|V^{\mathrm{C}}_{-\mathbf{G},z_\mathrm{p}+z}\, \mathrm{e}^{-\mathrm{i}\mathbf{G}\cdot(\mathbf{R}+\mathbf{R}_\mathrm{p})}|\beta\rangle$$

connects states $|\alpha\rangle$ and $|\beta\rangle$ *via* the harmonic $\mathbf{G}$ of the crystal potential; the rates $\Gamma_{\alpha\beta}$ account for the leakage of electron probability due to both coherent excitation to the continuum (i.e., CL),

$$\Gamma^{\mathrm{CL}}_{\alpha\beta} = 2\pi \sum_{k\in Q}\sum_{\mathbf{G}} \langle\alpha|V^{\mathrm{C}}_{\mathbf{G},z_\mathrm{p}+z}\, \mathrm{e}^{\mathrm{i}\mathbf{G}\cdot\mathbf{R}}|k\rangle\langle k|V^{\mathrm{C}}_{-\mathbf{G},z_\mathrm{p}+z}\, \mathrm{e}^{-\mathrm{i}\mathbf{G}\cdot\mathbf{R}}|\beta\rangle\delta(\varepsilon_k - \varepsilon_\beta - \mathbf{G}\cdot\mathbf{v}), \tag{9}$$

and incoherent electron–electron Auger processes,

$$\Gamma^{\mathrm{Auger}}_{\alpha\beta} = \sum_\mu \int_0^\infty \frac{\mathrm{d}\omega}{2\pi} \int \frac{\mathrm{d}\mathbf{q}}{(2\pi)^3} \frac{16\pi^2}{q^2} \mathrm{Im}\left\{\frac{-1}{\varepsilon(q,\omega)}\right\} \times \langle\alpha|\mathrm{e}^{\mathrm{i}\mathbf{q}\cdot\mathbf{r}}|\mu\rangle\langle\mu|\mathrm{e}^{-\mathrm{i}\mathbf{q}\cdot\mathbf{r}}|\beta\rangle\delta(\varepsilon_\mu - \varepsilon_\beta + \omega - \mathbf{q}\cdot\mathbf{v}); \tag{10}$$

and

$$V_{\alpha\beta} = -\langle\alpha|\bar{V}^{\mathrm{C}} + (Z_1 - 1/2)\phi_{\mathrm{wake}}|\beta\rangle, \tag{11}$$

where ϕ_{wake} is the wake potential induced by a unit charge [5,68,69]. The 1/2 term stands for the electron self-interaction. In the case of surface channeling, ϕ_{wake} may have a smooth dependence on the time, introduced through the surface-atom separation, but even in planar channeling it will contain a z_p dependence due to the different charge density of valence electrons for different positions across the channel, since deeply bound target electrons will also give a small contribution to the induced potential.

3. DYNAMICAL MIXING OF ELECTRONIC STATES

RCE is produced by the second term in the right-hand side of equation (7). In our picture, the energies ε_α are time independent. However, we can define an adiabatic basis set obtained by diagonalizing the first term in the right-hand side of equation (7)

$$\sum_\beta V_{\alpha\beta} a_\beta^\lambda = (E_\lambda - \varepsilon_\alpha) a_\alpha^\lambda, \tag{12}$$

where a_α^λ is the projection of perturbed state $|\phi_\lambda\rangle$ (of energy E_λ) on to unperturbed state $|\alpha\rangle$ (of energy ε_α). Then, the energies of this adiabatic basis set of states depend on the position of the ion relative to the channel, and therefore, they evolve with time as the ion moves along the channel. This is schematically depicted in Fig. 1, where one can see that the condition for RCE occurs at specific values of the position of the ion with respect to the crystal atomic walls.

The dependence of the adiabatic states on the ion position is due to both the crystal potential and the induced wake potential (equation (11)). The crystal potential has been calculated by summing up the contributions coming from all target atoms in the Ziegler, Biersack, and Littmark approximation [70,71]. This neglects many-body effects in the crystal potential that are not so important in this context because of the electron-transition energies under consideration.

For the wake potential, a dielectric formalism has been followed [5,68] (also to obtain Auger matrix elements [5,69]). Use has been made of the random-phase-approximation dielectric function [72] for a homogeneous electron gas of density corresponding to the average over the ion trajectory along several target atom spacings. For surface channeling, the situation is more complicated due to the role played by collective surface excitations (surface plasmons) in the induced potential. This is clearly observed in the induced wake potential produced by a point charge moving parallel to an aluminum surface for different impact parameters of the charge relative to the surface, as shown in Fig. 2. Oscillations of frequency $\omega_s = \omega_p/\sqrt{2}$ (surface plasma frequency) are observed outside the metal ($z > 0$), whereas bulk plasma oscillations of frequency ω_p show up as well when the charge is moving inside the medium.

A specific example of adiabatic-state energies that will become useful later on is shown in Fig. 3 for Mg^{11+} hydrogen-like ions moving with a velocity of 31.6 a.u. in a (100) channel of a Ni crystal. The relevant states within the P subspace are those of the K and L shells of the ion. In particular, L states are degenerate outside the crystal and they are mixed and energy shifted due to the noted interaction. Figure 3 represents the energy difference between the 1s state and the adiabatic states of the L shell. The p state

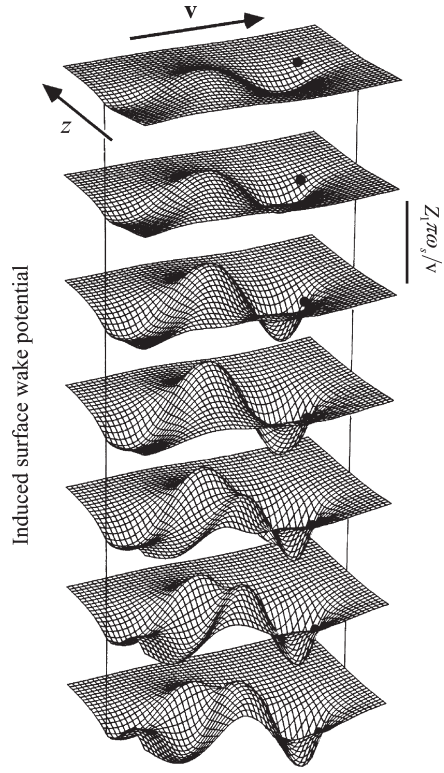

Fig. 2. Induced surface wake potential created by a charged particle of charge Z_1 moving with constant velocity $v = 2$ a.u. parallel to an aluminum surface for various impact parameters: $z/L = 0.4$, 0.2, 0, -0.2, -0.4, -0.6, and -0.8 (from top to bottom), where $L = \pi v/2\omega_s$ (4.04 Å) and ω_s is the surface plasmon energy. The surface, represented by vertical lines, is placed at $z = 0$. Each grid extends from $z = -L$ to L along the surface normal, and from $x = -4L$ to L along the direction of motion. The subdivisions in the grids correspond to squares of side $L/10$. The particle (black circles) is located at $x = 0$ and is moving from left to right.

perpendicular to the paper does not mix with the other L states. However, a complex pattern of evolution is observed for the mixing of the latter. The actual shape of the four adiabatic states of the L shell is shown in the insets. Notice that the state $\lambda = 1$ is oriented towards the channel wall, and consequently, it can be more easily populated by RCE than the rest [34].

Under the same conditions as in Fig. 3 the impact-parameter dependence of transition rates (9) and (10), are represented in Fig. 4 in order to illustrate the interplay between coherent (Γ^{CL}, solid curves) and Auger (Γ^{AL}, dashed curves) electron-loss mechanisms: incoherent Auger processes are dominant near the channel mid-planes, whereas coherent ionization dominates in

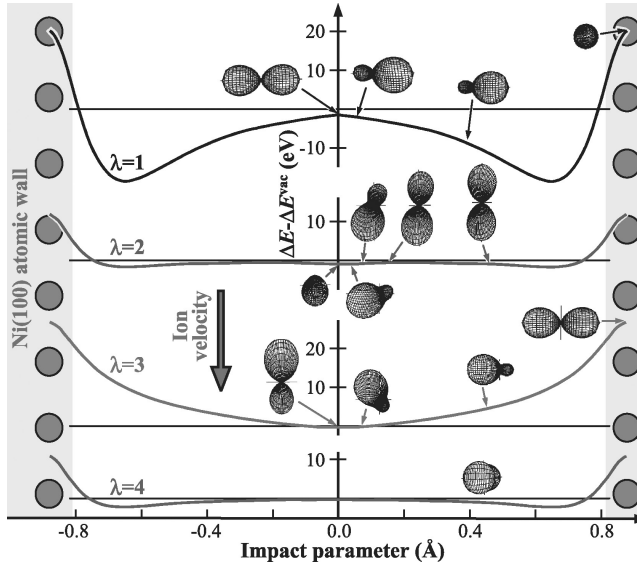

Fig. 3. Transition energies between the 1s state and the hybrid adiabatic states of the L shell of a 25 MeV/amu Mg^{11+} ion moving parallel to a (100) planar channel of a Ni crystal as a function of distance from the channel mid-plane (impact parameter). The energy differences ΔE are given relative to the vacuum value, ΔE^{vac}. The shape of the electronic wave function of the different excited states is shown for various positions in the channel by means of the accompanying insets. They represent the radial integral of the squared electron wave function. The ion moves from top to bottom.

the vicinity of the atomic walls. The rate of Auger excitation is also shown for completeness (Γ^{AE}, dot-dashed curves). The latter can be in turn divided into Auger loss (AL) and Auger (de-)excitation (AE) to different bound states: $\Gamma_{\alpha\beta}^{\mathrm{Auger}} = \Gamma_{\alpha\beta}^{\mathrm{AL}} + \Gamma_{\alpha\beta}^{\mathrm{AE}}$, depending whether the state k lies in the continuum of the ion or in any of its excited states. These two contributions are of the same order of magnitude.

4. RESONANT-COHERENT EXCITATION TO THE CONTINUUM

Let us analyze in more detail the CL processes described by equation (9). It is convenient to notice that only some **G** vectors contribute significantly, since form factors like $\langle\alpha|V_{\mathbf{G},z_{\mathrm{p}}+z}\,\mathrm{e}^{\mathrm{i}\mathbf{G}\mathbf{R}}|k\rangle$ take very small values unless $(k_x, k_y) \simeq \mathbf{G}$, and this condition can be made consistent with the conservation of energy, expressed through the δ function, only for specific **G** vectors. This has been taken into account in the calculation of the CL rate shown in Fig. 4.

For planar or surface channeling, the direction of emission of the lost electrons can be obtained from the construction shown in Fig. 5. This is

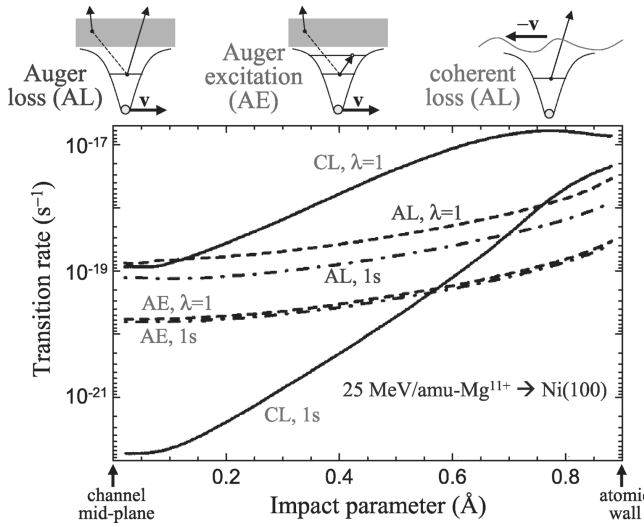

Fig. 4. Impact-parameter dependence of the transition rates involving 1s and $\lambda = 1$ states (see Fig. 3). Γ^{CL} (coherent-loss; solid curves), Γ^{AL} (Auger loss, which is a part of equation (10); dashed curves), and Γ^{AE} (Auger excitation, the remaining part of equation (10); dot-dashed curves) are calculated under the same conditions as in Fig. 3. The insets above the plot are intended to show schematically the processes under consideration.

similar to momentum transfer in low-energy electron diffraction [73], except that the ejected electrons are now represented by a distribution that is centered around the ion velocity in momentum space. The width of such distribution is determined by the Fourier transform of the bound electron initial wave function, and it is of the order of $1/Z_1$, which is typically smaller than the distance between adjacent $\mathbf{G}$ points.

This means that CL can produce the emission of electrons with well-defined momentum along preferential directions. This is actually the case shown in Fig. 6. A detailed calculation of the trajectory and the corresponding time-evolution of the electronic states of the ion has been performed to obtain the data represented in the figure [66]. This corroborates the idea that CL leads to preferential directions of emission.

5. FULL CALCULATION AND COMPARISON WITH EXPERIMENT

The electron evolves non-adiabatically in part, in the sense that the excited electron wave function retains during long times (of the order of the period

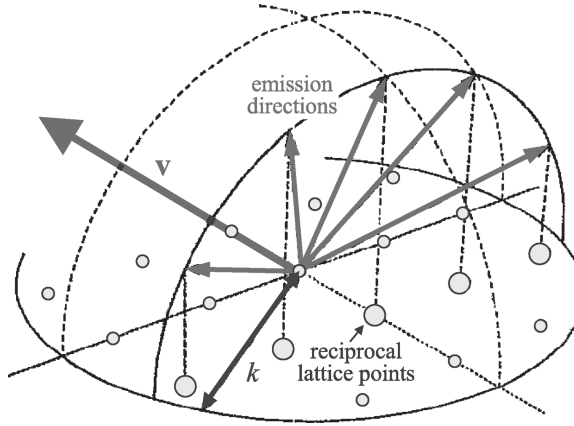

Fig. 5. Schematic construction of the direction of emission in the coherent loss process for surface or planar channeling. The reciprocal lattice vectors of the surface or plane, **G**, are represented by hollow circles (see equation (9)). The construction makes use of the sphere of constant electron momentum k in the rest frame of the ion. Coherently lost electrons are promoted to such sphere and the directions of emission are preferentially given by the points whose projection on the surface or plane coincides with one of the **G** vectors.

of the trajectory oscillations in the channel) the character of the original adiabatic state to which it was promoted [63]. So, the features associated to RCE can only be fully understood through a detailed calculation that incorporates the time evolution of the ion trajectory and its electronic state.

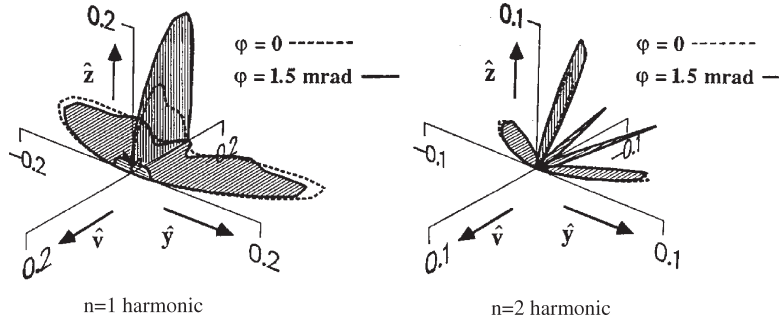

Fig. 6. Angular distribution of coherently emitted electrons after scattering of 2.5 MeV He^+ ions on a W(100) surface with two different grazing angles of incidence (see labels). The ions are directed along a ⟨100⟩ azimuthal direction. The emission is shown for the two first crystal-potential harmonics ($\mathbf{G}\cdot\mathbf{v} = 2\pi n v/a$, where $n = 1-2$ and $a = 3.16$ Å is the lattice constant) along the direction of motion.

The electron transition energy of resonance $\Delta E_{\rm res}$ depends on the orientation of the trajectory *via* $\mathbf{G}\cdot\mathbf{v}$ (see equation (7)). For an ion moving parallel to a (100) surface or planar channel of an fcc crystal, like that considered in Fig. 3, one has

$$\frac{\Delta E_{\rm res} a}{2\pi v\gamma} = k\cos\varphi + l\sin\varphi, \tag{13}$$

where $\gamma = 1/\sqrt{1 - c^2/v^2}$ accounts for the relativistic Lorentz contraction of the lattice constant a, φ is the angle between the ion velocity and a $\langle 100\rangle$ direction, and (k, l) are integers such that $k + l$ is an even number. Equation (13) can be combined with the data displayed in Fig. 3 to obtain the impact parameter at which the resonance condition is fulfilled as a function of the angle φ [62]. For example, for $\varphi = 26.2°$ the $\lambda = 1$ state of Fig. 3 is in resonance with the 1s state at the impact parameter indicated by the dotted lines of Fig. 7.

The Schrödinger equation (7) has been solved numerically for a trajectory corresponding to the dashed line shown in Fig. 7. The Auger and RCL processes have been neglected for simplicity and the ion trajectory has been calculated using the ZBL inter-atomic potential. The electron of the hydrogenic Mg^{11+} ions under consideration was initially prepared in the ground state 1s. The solid line shows the probability of finding the electron in

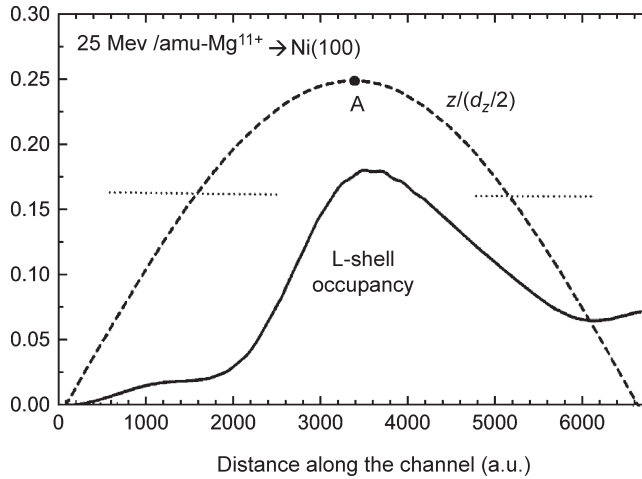

Fig. 7. Under the same conditions as in Fig. 3, the probability of occupancy of the L shell (solid curve) is shown along the trajectory of the ion (dashed curve) when the ion velocity forms an angle $\varphi = 26.2°$ with respect to a $\langle 100\rangle$ direction within the plane. The projectile is prepared in the 1s state initially. The dotted horizontal bars indicate the impact parameter of the resonance with the $\lambda = 1$ state.

an excited state within the L shell as a function of the distance along the direction parallel to the channel. Notice that RCE occurs after the ion has crossed the resonance. A more detailed analysis of this particular example shows that the evolution of the electron as the ion evolves in the channel is not adiabatic [62], and this explains partly why the occupancy does not change suddenly at the resonant impact parameters. On the way back to the channel mid-plane, the resonant-coherent interaction acts in the sense of reducing the population of excited states (resonant-coherent de-excitation).

This reduction can be complete for certain impact parameters z_A, as shown in Fig. 8, where the occupancy of the L shell at the end of the trajectory shown in the inset is shown for an ion initially prepared in the ground state 1s. Each point of the curve corresponds to a different trajectory as a function of the trajectory amplitude z_A. The oscillations observed in the figure are familiar in the study of potential-curve crossing of low-energy ions [74].

Finally, Fig. 9 represents the probability that a Mg^{11+} ion survives after crossing a thin Ni film as shown in the inset (i.e., Mg^{11+} fraction on exit). By changing the angle within the planar channel, one can tune the energy of resonance according to equation (13), giving rise to the structure shown in the figure [63]. In the calculation, the beam has been considered to enter the film parallel to the channel planes with no divergence. An average

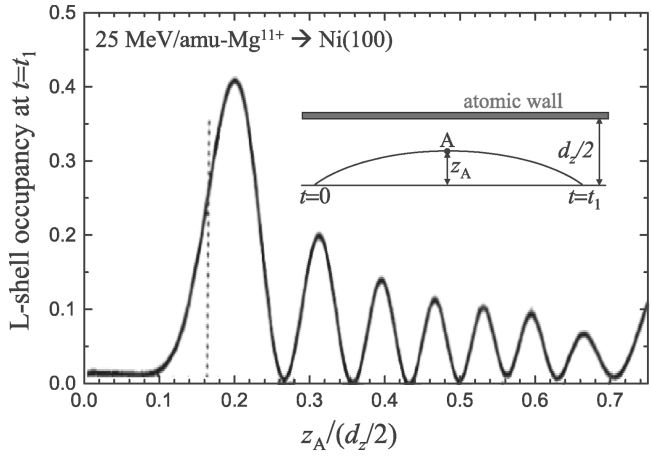

Fig. 8. Probability that an electron prepared in the ground state at time $t = 0$ is in the L shell at time $t = t_1$ due to RCE for different impact parameters z_A, under the same conditions as in Fig. 3. The ion trajectory is schematically shown in the inset. The angle with respect to a $\langle 100 \rangle$ direction within the plane has been taken $\varphi = 26.2°$. The dotted line shows the distance at which the state $\lambda = 1$ in Fig. 3 is in resonance with the (2,0) harmonic (see equation (13)). Finally, d_z represents the channel width.

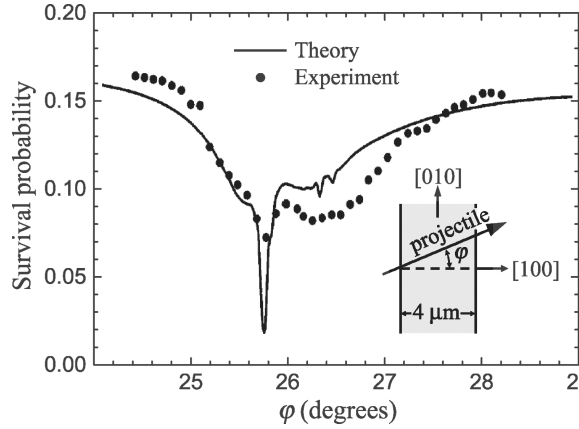

Fig. 9. Survival fraction of 25 MeV/amu Mg^{11+} ions after passing through a (100) planar channel of a 4000 Å thick Ni single crystal. φ is the angle between the velocity and a $\langle 100 \rangle$ direction within the channel plane. The inset represents a top view of the channel. The faces of the crystal are perpendicular to that direction. Solid line: present theory, multiplied by a factor of 0.3 to fit the experimental point corresponding to $\varphi = 28°$. Circles: experiment [34].

over initial impact parameters has been performed. The agreement between theory and experiment is relatively good, and the main features of the survival probability curve are well reproduced.

ACKNOWLEDGEMENTS

This work has been partially supported by the Basque Departamento de Educación, Universidades e Investigación, the University of the Basque Country UPV/EHU (Contract No. 00206.215-13639/2001), and the Spanish Ministerio de Ciencia y Tecnología (Contract No. MAT2001-0946).

APPENDIX A. COUPLED CHANNEL EQUATIONS FOR THE RELEVANT BOUND STATES

This appendix describes the steps required to obtain equation (7). An electron originally bound to the ion will be singled out in what follows, and it is the evolution of this electron that we shall be considering.

Let us start by introducing in the states of the electron–target system an explicit dependence both on the target state n and on the quantum numbers of the relevant electron. The index of the latter will be denoted α for a subset

of electron states bound to the ion, k for the rest of states, and μ for both of them. Then, the matrix elements of the ion–target interaction operator that appears in the coupled-channel set of equations (6) take the form, according to equation (3),

$$\langle \mu n|\hat{U}|\mu' n'\rangle = \frac{1}{A}\sum_{\mathbf{Q}} \mathrm{e}^{\mathrm{i}\mathbf{Q}\cdot(\mathbf{R}_\mathrm{p}+\mathbf{v}t)}[Z_1\delta_{\mu\mu'}\langle n|V_{\mathbf{Q},z_\mathrm{p}}|n'\rangle - \langle \mu n|V_{\mathbf{Q},z_\mathrm{p}+z}\,\mathrm{e}^{\mathrm{i}\mathbf{Q}\cdot\mathbf{R}}|\mu' n'\rangle], \tag{A1}$$

where $V_{\mathbf{Q},z_\mathrm{p}}$ is the interaction potential in momentum space along the directions parallel to the channel plane or surface and A is the area of the entire surface (or plane). In particular, for elastic channels (i.e., $n = n' = 0$) one finds

$$\langle \mu 0|\hat{U}|\mu' 0\rangle = \sum_{\mathbf{G}} \mathrm{e}^{\mathrm{i}\mathbf{G}\cdot(\mathbf{R}_\mathrm{p}+\mathbf{v}t)}[Z_1\delta_{\mu\mu'}V^\mathrm{C}_{\mathbf{G},z_\mathrm{p}} - \langle \mu|V^\mathrm{C}_{\mathbf{G},z_\mathrm{p}+z}\,\mathrm{e}^{\mathrm{i}\mathbf{G}\cdot\mathbf{R}}|\mu'\rangle],$$

where $V^\mathrm{C}_{\mathbf{G},z}$ are Fourier components of the crystal potential (see equation (4)). The lattice symmetry is reflected in the use of 2D reciprocal lattice vectors, $\mathbf{G}$. Notice that $\langle \mu n|\hat{U}|\mu' n'\rangle$ does not possess this symmetry, in general, for excited states of the target $|n\rangle$ and $|n'\rangle$, so that the summation over $\mathbf{Q}$ in equation (A1) is dense.

Now, we proceed to integrate equation (6) for the states of the subset Q considered in Section 2 (i.e., $|\mu n\rangle$, with $n \neq 0$, and $|k0\rangle$ with k belonging to Q) over a time interval $\Delta t = t - t_0$, assuming that only P states $|\alpha 0\rangle$ contribute to the right-hand side of the equation (first-order perturbation theory). In other words, the occupancy of Q states will be considered to be much smaller than that of $|\alpha 0\rangle$, since coherence is quickly lost during the evolution of the electron in the former. Furthermore, it will be assumed that $z_b(t)$, and hence also the crystal potential at the position of the ion, does not change significantly during the time interval Δt. Finally, $a_{\alpha 0}$ will be taken to remain practically constant during that period of time [75]. Then, one finds

$$a_{\mu,n>0} = \frac{-1}{A}\sum_{\alpha,\mathbf{Q}} a_{\alpha 0}[Z_1\delta_{\mu\alpha}\langle n|V_{\mathbf{Q},z_\mathrm{p}}|0\rangle - \langle \mu n|V_{\mathbf{Q},z_\mathrm{p}+z}\,\mathrm{e}^{\mathrm{i}\mathbf{Q}\cdot\mathbf{R}}|\alpha 0\rangle] \times \mathrm{e}^{\mathrm{i}\mathbf{Q}\cdot\mathbf{R}_\mathrm{p}}\frac{\mathrm{e}^{\mathrm{i}(\varepsilon_{\mu n}-\varepsilon_{\alpha 0}+\mathbf{Q}\cdot\mathbf{v})t} - \mathrm{e}^{\mathrm{i}(\varepsilon_{\mu n}-\varepsilon_{\alpha 0}+\mathbf{Q}\cdot\mathbf{v})t_0}}{\varepsilon_{\mu n} - \varepsilon_{\alpha 0} + \mathbf{Q}\cdot\mathbf{v}},$$

and

$$a_{k0} = \sum_{\alpha,\mathbf{G}} a_{\alpha 0}\langle k|V^\mathrm{C}_{\mathbf{G},z_\mathrm{p}+z}\,\mathrm{e}^{\mathrm{i}\mathbf{G}\cdot\mathbf{R}}|\alpha\rangle \mathrm{e}^{\mathrm{i}\mathbf{G}\cdot\mathbf{R}_\mathrm{p}}\frac{\mathrm{e}^{\mathrm{i}(\varepsilon_{k0}-\varepsilon_{\alpha 0}+\mathbf{G}\cdot\mathbf{v})t} - \mathrm{e}^{\mathrm{i}(\varepsilon_{k0}-\varepsilon_{\alpha 0}+\mathbf{G}\cdot\mathbf{v})t_0}}{\varepsilon_{k0} - \varepsilon_{\alpha 0} + \mathbf{G}\cdot\mathbf{v}}.$$

Substituting these amplitudes back into equation (6) and taking the $\Delta t \to \infty$ limit, consistent with trajectories nearly parallel to the channel,

one obtains

$$\mathrm{i}\frac{\mathrm{d}a_\alpha}{\mathrm{d}t} = \sum_\beta a_\beta (A_{\alpha\beta} + B_{\alpha\beta} + C_{\alpha\beta}), \tag{A2}$$

where $a_{\alpha 0}$ has been abbreviated as a_α,

$$A_{\alpha\beta} = \sum_{\mathbf{G}} \mathrm{e}^{\mathrm{i}(\varepsilon_\alpha - \varepsilon_\beta - \mathbf{G}\cdot\mathbf{v})t}\, \mathrm{e}^{-\mathrm{i}\mathbf{G}\cdot\mathbf{R}_\mathrm{p}} [Z_1 \delta_{\alpha\beta} V^\mathrm{C}_{-\mathbf{G},z_\mathrm{p}} - \langle\alpha| V^\mathrm{C}_{-\mathbf{G},z_\mathrm{p}+z}\, \mathrm{e}^{-\mathrm{i}\mathbf{G}\cdot\mathbf{R}} |\beta\rangle], \tag{A3}$$

$$B_{\alpha\beta} = -\mathrm{i}\pi \sum_{\mathbf{G}\mathbf{G}'} \sum_k \mathrm{e}^{\mathrm{i}(\varepsilon_\alpha - \varepsilon_\beta - \mathbf{G}'\cdot\mathbf{v})t}\, \mathrm{e}^{-\mathrm{i}\mathbf{G}'\cdot\mathbf{R}_\mathrm{p}} \delta(\varepsilon_k - \varepsilon_\beta - \mathbf{G}\cdot\mathbf{v}) \times \langle\alpha| V^\mathrm{C}_{\mathbf{G}-\mathbf{G}',z_\mathrm{p}+z}\, \mathrm{e}^{\mathrm{i}(\mathbf{G}-\mathbf{G}')\cdot\mathbf{R}} |k\rangle\langle k| V^\mathrm{C}_{-\mathbf{G},z_\mathrm{p}+z}\, \mathrm{e}^{-\mathrm{i}\mathbf{G}\cdot\mathbf{R}} |\beta\rangle, \tag{A4}$$

and

$$C_{\alpha\beta} = -\frac{\mathrm{i}\pi}{A^2} \sum_{\mathbf{Q}\mathbf{Q}'} \sum_{\mu, n>0} \mathrm{e}^{\mathrm{i}(\varepsilon_\alpha - \varepsilon_\beta - \mathbf{Q}'\cdot\mathbf{v})t}\, \mathrm{e}^{-\mathrm{i}\mathbf{Q}'\cdot\mathbf{R}_\mathrm{p}} \delta(\varepsilon_{\mu n} - \varepsilon_{\beta 0} - \mathbf{Q}\cdot\mathbf{v}) \times [Z_1 \delta_{\alpha\mu} \langle 0| V_{\mathbf{Q}-\mathbf{Q}',z_\mathrm{p}} |n\rangle - \langle\alpha 0| V_{\mathbf{Q}-\mathbf{Q}',z_\mathrm{p}+z}\, \mathrm{e}^{\mathrm{i}(\mathbf{Q}-\mathbf{Q}')\cdot\mathbf{R}} |\mu n\rangle] \times [Z_1 \delta_{\beta\mu} \langle n| V_{-\mathbf{Q},z_\mathrm{p}} |0\rangle - \langle\mu n| V_{-\mathbf{Q},z_\mathrm{p}+z}\, \mathrm{e}^{-\mathrm{i}\mathbf{Q}\cdot\mathbf{R}} |\beta 0\rangle]. \tag{A5}$$

The identity

$$\lim_{\Delta t\to\infty} \frac{1 - \mathrm{e}^{-\mathrm{i}\Delta E \Delta t}}{\Delta E} = \mathrm{i}\pi\delta(\Delta E),$$

has been used to derive these expressions taking $\Delta E = \varepsilon_{\mu n} - \varepsilon_{\beta 0} - \mathbf{Q}\cdot\mathbf{v}$ in equation (A5) and $\Delta E = \varepsilon_k - \varepsilon_\beta - \mathbf{G}\cdot\mathbf{v}$ in equation (A4).

The terms proportional to Z_1 in equation (A3) and Z_1^2 in equation (A5) are independent of the electron state, and therefore they represent an overall energy shift that can be disregarded in the present analysis. The remaining terms in equations (A3)–(A5) permit us to reduce equation (A2) to the form of equation (7). More precisely,

(1) $A_{\alpha\beta}$. The last summation on the right-hand side of equation (7) comes from the remaining term in equation (A3), which contains the oscillatory perturbation that leads to RCE. The part of that sum over reciprocal lattice vectors such that $\mathbf{G}\cdot\mathbf{v} = 0$ permits defining a continuous channel potential that enters equations (7) and (8) *via* the first term in equation (11).
(2) $B_{\alpha\beta}$. When α and β have very different energy (e.g., if one of them belongs to the K shell and the other to the L shell), $B_{\alpha\beta}$ represents a small contribution to $\alpha \rightarrow \beta$ transitions involving non-resonant

intermediate states in the continuum, k. However, when their energy difference is small (i.e., if either $\alpha = \beta$ or they belong to the L shell), $B_{\alpha\beta}$ describes RCE of the electron to the continuum ($\mathbf{G}' = 0$ term), and it can be recast as the self-energy contribution given by equation (9).

(3) $C_{\alpha\beta}$. This term gives rise to non-resonant contributions coming from the excitation and polarization of the target. In particular, the part proportional to Z_1 can be expressed in terms of the so-called wake potential [5,68], whereas the remaining part describes excitations of the electron to the continuum due to the screened interaction with the target. We will approximate the response of the target by that of an infinite electron gas with density equal to the time-averaged local density at the position of the moving ion. Then, the summation over target excitations can be dumped into the dielectric function of such an electron gas, $\varepsilon(\mathbf{q}, \omega)$, using the well-known relation [76]

$$\mathrm{Im}\left\{\frac{-1}{\varepsilon(\mathbf{q},\omega)}\right\} = \frac{4\pi^2}{q^2}\sum_n |\langle 0|\rho(\mathbf{q})|n\rangle|^2 \delta(\omega - \omega_{n0}), \qquad \omega > 0,$$

where ρ is the electron density operator and ω_{n0} are excitation energies. Working in 3D momentum space $\mathbf{q}$ with real space volume Ω and retaining only $\mathbf{q}' = 0$ terms (this assumes translational invariance in the response function), one finds from equation (A5)

$$C_{\alpha\beta} = -\frac{\mathrm{i}}{2\Omega}\sum_{\mathbf{q}}\int_0^\infty \frac{\mathrm{d}\omega}{2\pi}\frac{16\pi^2}{q^2}\sum_\mu \mathrm{e}^{\mathrm{i}(\varepsilon_\alpha - \varepsilon_\beta)t}\delta(\varepsilon_\mu - \varepsilon_\beta + \omega - \mathbf{q}\cdot\mathbf{v})$$
$$\times \mathrm{Im}\left\{\frac{-1}{\varepsilon(\mathbf{q},\omega)}\right\}[Z_1\delta_{\alpha\mu} - \langle\alpha|\mathrm{e}^{\mathrm{i}\mathbf{q}\cdot\mathbf{r}}|\mu\rangle][Z_1\delta_{\beta\mu} - \langle\mu|\mathrm{e}^{-\mathrm{i}\mathbf{q}\cdot\mathbf{r}}|\beta\rangle],$$

which yields a real potential proportional to Z_1 acting on the electron, as written in equation (11) in terms of the wave potential, and a contribution to the self-energy *via* Auger transitions (equation (10)).

REFERENCES

[1] S. Datz, C. D. Moak, O. H. Crawford, H. F. Krause, P. F. Dittner, J. G. del Campo, J. A. Biggerstaff, P. D. Miller, P. Hvelplund and H. Knudsen, *Phys. Rev. Lett.*, 1978, **40**, 843.
[2] C. D. Moak, S. Datz, O. H. Crawford, H. F. Krause, P. F. Dittner, J. G. del Campo, J. A. Biggerstaff, P. D. Miller, P. Hvelplund and H. Knudsen, *Phys. Rev. B*, 1979, **19**, 977.
[3] S. Datz, *J. Physique Colloque*, 1979, **40**, C1.
[4] S. Datz, C. D. Moak, O. H. Crawford, H. F. Krause, P. D. Miller, P. F. Dittner, J. G. del Campo, J. A. Biggerstaff, H. Knudsen and P. Hvelplund, *Nucl. Instrum. Methods Phys. Res. B*, 1980, **170**, 15.
[5] P. M. Echenique, F. Flores and R. H. Ritchie, *Solid State Phys.*, 1990, **43**, 229.
[6] F. J. García de Abajo and J. M. Pitarke, *Nucl. Instrum. Methods Phys. Res. B*, 1994, **90**, 222.
[7] V. V. Okorokov, *JETP Lett.*, 1965, **2**, 111.

[8] V. V. Okorokov, D. L. Tolchenkov, I. S. Khizhnyakov, Y. N. Cheblukov, Y. Y. Lapitski, G. A. Iferov and Y. N. Zhukova, *JETP Lett.*, 1972, **16**, 415.
[9] V. V. Okorokov, D. L. Tolchenkov, I. S. Khizhnyakov, Y. N. Cheblukov, Y. Y. Lapitski, G. A. Iferov and Y. N. Zhukova, *Phys. Lett. A*, 1973, **43**, 485.
[10] M. J. Gaillard, J.-C. Poizat, J. Remillieux and M. L. Gaillard, *Phys. Lett. A*, 1973, **45**, 306.
[11] H. G. Berry, D. S. Gemmell, R. E. Holland, J.-C. Poizat, J. Remillieux and J. N. Worthington, *Phys. Lett. A*, 1974, **49**, 123.
[12] M. Mannami, H. Kudo, M. Matsushita and K. Ishii, *Phys. Lett. A*, 1977, **64**, 136.
[13] M. J. Gaillard, J.-C. Poizat, J. Remillieux, A. Chateau-Thierry, A. Gladieux and W. Brandt, *Nucl. Instrum. Methods*, 1976, **132**, 547.
[14] T. Azuma, K. Komaki, M. Yamagata, Y. Yamazaki, M. Sekiguchi, T. Hattori and T. Hasegawa, *Nucl. Instrum. Methods Phys. Res. B*, 1996, **115**, 310.
[15] K. Kimura, Y. Fujii, M. Hasegawa, Y. Susuki and M. Mannami, *Phys. Rev. B*, 1988, **38**, 1052.
[16] K. Kimura, H. Ohtsuka and M. Mannami, *Phys. Rev. Lett.*, 1992, **68**, 3797.
[17] C. Auth, A. Mertens, H. Winter, A. G. Borisov and F. J. García de Abajo, *Phys. Rev. Lett.*, 1997, **79**, 4477.
[18] H. Winter, R. Kirsch and J. C. Poizat, *Phys. Rev. A*, 1991, **67**, R1660.
[19] C. Auth and H. Winter, *Phys. Rev. A*, 2000, **62**, 12903.
[20] H. Winter, C. Auth and T. Hecht, *Vacuum*, 2002, **66**, 137.
[21] T. Hecht and H. Winter, *Phys. Lett. A*, 1998, **243**, 306.
[22] K. Kimura, Y. Fujii, M. Hasegawa, Y. Susuki and M. Mannami, *Phys. Rev. B*, 1988, **38**, 1052.
[23] Y. Fujii, K. Sueoka, K. Kimura and M. Mannami, *J. Phys. Soc. Jpn*, 1989, **58**, 2758.
[24] Y. Fujii, K. Sueoka, K. Kimura and M. Mannami, *Radiat. Effects*, 1990, **114**, 239.
[25] Y. Fujii, S. Fujiwara, K. Kimura and M. Mannami, *Nucl. Instrum. Methods Phys. Res. B*, 1991, **58**, 18.
[26] K. Narumi, Y. Fujii, K. Toba, K. Kimura and M. Mannami, *Nucl. Instrum. Methods Phys. Res. B*, 1995, **100**, 1.
[27] K. Kimura, H. Ida, M. Fritz and M. Mannami, *Phys. Rev. Lett.*, 1996, **76**, 3850.
[28] M. Mannami, K. Kimura, K. Narumi, M. Yamamoto and S. Naito, *Nucl. Instrum. Methods Phys. Res. B*, 1997, **125**, 97.
[29] K. Kimura and M. Mannami, *Phys. Rev. A*, 1998, **57**, 1121.
[30] K. Kimura, S. Ooki, H. Ida and M. Mannami, *Nucl. Instrum. Methods Phys. Res. B*, 1998, **135**, 419.
[31] H. F. Krause, S. Datz, P. F. Dittner, N. L. Jones and C. R. Vane, *Phys. Rev. Lett.*, 1993, **71**, 348.
[32] H. F. Krause, J. H. Barrett, S. Datz, P. F. Dittner, N. L. Jones, J. G. del Campo and C. R. Vane, *Phys. Rev. A*, 1994, **49**, 283.
[33] S. Datz, H. F. Krause and C. R. Vane, *Nucl. Instrum. Methods Phys. Res. B*, 1996, **115**, 363.
[34] S. Datz, P. F. Dittner, H. F. Krause, C. R. Vane, O. H. Crawford, J. S. Forster, G. S. Ball, W. G. Davies and J. S. Geiger, *Nucl. Instrum. Methods Phys. Res. B*, 1995, **100**, 272.
[35] N. Hatke, M. Dirska, M. Grether, E. Luderer, A. Robin, A. Nrmann and W. Heiland, *Phys. Rev. Lett.*, 1997, **79**, 3395.
[36] N. Hatke, M. Dirska, E. Luderer, A. Robin, M. Grether, A. Närmann and W. Heiland, *Nucl. Instrum. Methods Phys. Res. B*, 1998, **135**, 307.
[37] F. Fujimoto, K. Komaki, A. Ootuka, E. Vilalta, Y. Iwata, Y. Hirao, T. Hasegawa, M. Sekiguchi, A. Mizobuchi, T. Hattori and K. Kimura, *Nucl. Instrum. Methods Phys. Res. B*, 1988, **33**, 354.

[38] S. Datz, P. F. Dittner, J. G. del Campo, K. Kimura, K. F. Krause, T. M. Rosseel and C. R. Vane, *Radiat. Effects*, 1991, **117**, 73.
[39] J. S. Forster, G. C. Ball, W. G. Davies, J. S. Geiger, J. U. Andersen, J. A. Davies, H. Geissel and F. Nickel, *Nucl. Instrum. Methods Phys. Res. B*, 1996, **115**, 363.
[40] T. Azuma, T. Ito, Y. Yamazaki, K. Komaki, M. Sano, M. Torikoshi, A. Kitagawa, E. Takada and T. Murakami, *Nucl. Instrum. Methods Phys. Res. B*, 1998, **135**, 61.
[41] K. Komaki, T. Azuma, T. Ito, Y. Takabayashi, Y. Yamazaki, M. Sano, M. Torikoshi, A. Kitagawa, E. Takada and T. Murakami, *Nucl. Instrum. Methods Phys. Res. B*, 1998, **146**, 19.
[42] K. Komaki, *Nucl. Instrum. Methods Phys. Res. B*, 1998, **135**, 16.
[43] T. Azuma, T. Ito, K. Komaki, Y. Yamazaki, M. Sano, M. Torikoshi, A. Kitagawa, E. Takada and T. Murakami, *Phys. Rev. Lett.*, 1999, **83**, 528.
[44] T. Azuma, Y. Takabayashi, T. Ito, K. Komaki, Y. Yamazaki, E. Takada and T. Murakami, *Nucl. Instrum. Methods Phys. Res. B*, 2003, **212**, 397.
[45] T. Ito, Y. Takabayashi, K. Komaki, T. Azuma, Y. Yamazaki, S. Datz, E. Takada and T. Murakamic, *Nucl. Instrum. Methods Phys. Res. B*, 2000, **164/165**, 68.
[46] T. Azuma, T. Muranaka, Y. Takabayashi, T. Ito, C. Kondo, K. Komaki, Y. Yamazaki, S. Datz, E. Takada and T. Murakami, *Nucl. Instrum. Methods Phys. Res. B*, 2003, **205**, 779.
[47] Y. Nakai, T. Ikeda, Y. Kanai, T. Kambara, N. Fukunishi, T. Azuma, K. Komaki, Y. Takabayashi and Y. Yamazaki, *Nucl. Instrum. Methods Phys. Res. B*, 2003, **205**, 784.
[48] J. Neufeld and R. H. Ritchie, *Phys. Rev.*, 1955, **98**, 1632.
[49] P. M. Echenique, R. H. Ritchie and W. Brandt, *Phys. Rev. B*, 1979, **20**, 2567.
[50] F. J. García de Abajo and P. M. Echenique, *Phys. Rev. B*, 1993, **48**, 13399.
[51] P. M. Echenique, F. J. García de Abajo, V. H. Ponce and M. E. Uranga, *Nucl. Instrum. Methods Phys. Res. B*, 1995, **96**, 583.
[52] S. Datz, C. D. Moak, T. S. Noggle, B. R. Appelton and H. O. Lutz, *Phys. Rev.*, 1969, **179**, 315.
[53] F. Abel, G. Amsel, M. Bruneaux, C. Cohen and A. L'Hoir, *Phys. Rev. B*, 1976, **13**, 993.
[54] O. H. Crawford and R. H. Ritchie, *Phys. Rev. A*, 1979, **20**, 1848.
[55] J. P. Rozet, A. Chetioui, P. Bouisset, D. Vernhet, K. Wohrer, A. Touati, C. Stephan and J. P. Grandin, *Phys. Rev. Lett.*, 1987, **58**, 337.
[56] K. Kimura, J. P. Gibbons, S. B. Elston, C. Biedermann, R. DeSerio, N. Keller, J. C. Levin, M. Breinig, J. Burgdörfer and I. A. Sellin, *Phys. Rev. Lett.*, 1991, **66**, 25.
[57] Y. Iwata, K. Komaki, Y. Yamazaki, M. Sekiguchi, T. Hattori, T. Hasegawa and F. Fujimoto, *Nucl. Instrum. Methods Phys. Res. B*, 1990, **48**, 163.
[58] Y. H. Ohtsuki, *Charged Beam Interaction with Solids*, Taylor & Francis, London, 1983.
[59] E. Kupfer, H. Gabriel and J. Burgdörfer, *Z. Phys.*, 1981, **300**, 35.
[60] J. Burgdörfer, H. Gabriel and E. Kupfer, *Nucl. Instrum. Methods*, 1982, **194**, 337.
[61] R. Kawai and M. Kawai, *Surf. Sci.*, 1988, **195**, 535.
[62] F. J. García de Abajo and P. M. Echenique, *Nucl. Instrum. Methods Phys. Res. B*, 1996, **115**, 299.
[63] F. J. García de Abajo and P. M. Echenique, *Phys. Rev. Lett.*, 1996, **76**, 1856.
[64] A. Salin, A. Arnau and P. M. Echenique, *Phys. Rev. B*, 1998, **57**, 2772.
[65] F. Sols and F. Flores, *Phys. Rev. B*, 1984, **30**, 4878.
[66] F. J. García de Abajo, V. H. Ponce and P. M. Echenique, *Phys. Rev. Lett.*, 1992, **69**, 2364.
[67] F. Guinea, F. Flores and P. M. Echenique, *Phys. Rev. Lett.*, 1981, **47**, 604.
[68] F. J. García de Abajo and P. M. Echenique, *Phys. Rev. B*, 1992, **46**, 2663.
[69] M. Rösler and F. J. García de Abajo, *Phys. Rev. B*, 1996, **54**, 17158.
[70] J. F. Ziegler, J. P. Biersack and U. Littmark, in *Proceedings of the International Ion Engineering Congress, ISIAT'83 & IPAT'83* (ed. J. F. Ziegler), Pergamon Press, New York, 1983, p. 1861.

[71] J. O'Connor and J. P. Biersack, *Nucl. Instrum. Methods Phys. Res. B*, 1986, **15**, 14.
[72] J. Lindhard, *K. Dan Vidensk. Selsk. Mat. Fys. Medd.*, 1954, **28** (8).
[73] J. B. Pendry, *Low Energy Electron Diffraction*, Academic Press, London, 1974.
[74] J. B. Delos and W. R. Thorson, *Phys. Rev. A*, 1972, **6**, 728.
[75] When $z_b(t)$ is such that the condition of RCE is fulfilled, the amplitudes $a_{\alpha 0}$ corresponding to states that are in resonance oscillate very rapidly. Under these circumstances, it can be proved that the final expressions derived in Appendix A and given in Section 2 remain valid as well.
[76] D. Pines and P. Nozières, *The Theory of Quantum Liquids*, W.A. Benjamin, New York, 1966.